RSC Advances

PAPER

View Article Online
View Journal | View Issue

Cite this: *RSC Adv.*, 2017, **7**, 7658

Novel $Bi_2O_2CO_3$/polypyrrole/g-C_3N_4 nanocomposites with efficient photocatalytic and nonlinear optical properties†

Wei Zhao,[a] Yun Wang,[b] Aijian Wang,*[b] Jun Qian,[b] Weihua Zhu,[b] Shengping Dou,[a] Qian Wang,*[a] Qin Zhong[c] and Aihua Chen[d]

Semiconductor nanostructures perform wide applications in light-driven physical and chemical processes; in particular, nanomaterials based on $Bi_2O_2CO_3$ with tunable photophysical properties have attracted intense interest. However, the nonlinear optical properties and photocatalytic performances of the ternary system $Bi_2O_2CO_3$/polypyrrole/g-C_3N_4 have not been reported. In this paper, a series of novel $Bi_2O_2CO_3$/polypyrrole/g-C_3N_4 nanocomposites loaded with different g-C_3N_4 contents was prepared to maximize the photocatalytic activity and optical nonlinearity. The structure, composition and morphology of the as-prepared samples were characterized by Fourier-transform infrared spectroscopy, X-ray powder diffraction, transmission electron microscopy, X-ray photoelectron spectroscopy and Raman spectroscopy. The wide absorption of the samples in the visible light region makes them suitable for photocatalytic and nonlinear transmission studies. Their photocatalytic performances were evaluated by degradation of rhodamine B. The associated photocatalytic activity of $Bi_2O_2CO_3$/polypyrrole/g-C_3N_4 nanocomposites is shown to be dependent on the g-C_3N_4 loading. Compared to $Bi_2O_2CO_3$, PPy, g-C_3N_4, BP and B/C0.5, the BP/C0.5 composite with 0.5 wt% g-C_3N_4 exhibits the highest photocatalytic activity. The nonlinear optical properties were investigated by open-aperture Z-scan measurements at 532 nm with 4 ns laser pulses. The results demonstrated that the BP/C0.5 composite exhibited improved properties for photocatalysis and optical nonlinearity, which is ascribed to a combination of mechanisms.

Received 18th December 2016
Accepted 11th January 2017

DOI: 10.1039/c6ra28346b

www.rsc.org/advances

1. Introduction

Nanomaterials exhibit changes in their physical and chemical properties with respect to their shape, size and composition. Nowadays, nanoelectronics is the most prevalent form of nanotechnology. Improvements in nanodevice performance are anticipated, which accounts for the extensive worldwide research efforts in the development of nanoscale material hybrids. Given their low price and abundant sources on Earth, bismuth-containing semiconductors have been attracting extensive attention over the past two decades.[1–5] Sillén-type $Bi_2O_2CO_3$ with alternating $Bi_2O_2^{2+}$ and CO_3^{2-} layers bears close resemblance to the Aurivillius-type oxides, which are important semiconductors that have long been used for medical and healthcare purposes.[6] Nevertheless, BiO_2CO_3 with the forbidden band width of *ca.* 3.3 eV can only absorb UV light, resulting in the low utilization efficiency of solar radiation.[1] According to the solar spectrum, UV light accounts for about 3–6% of the solar spectrum, whereas visible light comprises as much as 43%. Therefore, many scientists have paid much attention to how to broaden the photoabsorption region and improve the photocatalytic performance.[7–12] The conjugated polymers bearing π conjugated electron systems, such as polypyrrole (PPy) and their derivatives, have been shown great promises because of their high absorption coefficients in the visible range of the spectrum and highly efficient electron transport properties.[13,14] The conjugated structure and perfect conductivity of PPy can be useful to electron transfer during photocatalytic processes. Therefore, they can be used as a stable photosensitizer to modify semiconductors for improving photocatalytic efficiency. Graphitic carbon nitride (g-C_3N_4) is a novel metal-free photocatalyst with a band gap of *ca.* 2.8 eV, which is active for the degradation of some organic dyes such as rhodamine B under visible light irradiation,[15] and has been coupled with many semiconductor materials to hinder electron–hole pair recombination and enhance photocatalytic efficiency.[16,17]

[a]*School of Energy & Power Engineering, Jiangsu University, Zhenjiang 212013, P. R. China. E-mail: wajujs@ujs.edu.cn; qwang@ujs.edu.cn*

[b]*School of Chemistry & Chemical Engineering, Jiangsu University, Zhenjiang 212013, P. R. China*

[c]*School of Chemical Engineering, Nanjing University of Science and Technology, Nanjing 210094, P. R. China*

[d]*School of Chemistry & Chemical Engineering, Yancheng Institute of Technology, Yancheng 224051, P. R. China*

† Electronic supplementary information (ESI) available. See DOI: 10.1039/c6ra28346b

Meanwhile, the rapid development of nanoscience and nanotechnology provides lots of new opportunities for nonlinear optics. A growing number of nanomaterials have been shown to possess remarkable nonlinear optical properties, which promotes the design and fabrication of nanoscale optoelectronic and photonic devices in the field of optical limiting and optical switching.[18–20] Optical limiter is the optical component which reduces the laser beam intensity for the protection of eyes and light sensors. Nonlinear optical properties of nanoscale materials can be adjusted by changing their composition, and likewise, control of their optical limiting performance is desirable for high end applications.[21] Optical nonlinearity (including optical limiting) in individual nanoscale materials, *i.e.* carbon nitride nanotubes,[22] $Bi_2O_2CO_3$ (ref. 23) and PPy,[24] and coupled systems (hybrids) such as g-C_3N_4 functionalized with nine-atom silver quantum clusters,[25] zinc oxide doped bismuth[26] and transition metal oxide nanoparticles grafted graphitic g-C_3N_4 (ref. 27) have been reported. Similarly, the role of semiconductors functionalized g-C_3N_4 for photocatalytic applications is distinctive due to the fact that they are simulated sunlight active.[28] In view of the unique photoelectric properties of BiO_2CO_3, PPy and g-C_3N_4, it is of significant interest to design and prepare interesting functional materials combining the distinct optoelectronic properties of the individual components in suitable form. Particularly, the photocatalytic and nonlinear optical performances in coupled systems are expected to be better than those in independent systems due to the combination of the mechanisms (photocatalytic/nonlinear) occurring in the individual systems. To the best of our knowledge, there are no reports yet on the nonlinear optical properties and photocatalytic performances of the ternary system $Bi_2O_2CO_3$/polypyrrole/g-C_3N_4.

Based on the above considerations, herein, we report the preparation of a series of novel $Bi_2O_2CO_3$/PPy/g-C_3N_4 nanocomposites loaded with different g-C_3N_4 contents by a facile refluxing process. The composition and structure of the samples were investigated by means of Fourier transform infrared spectroscopy (FTIR), X-ray diffraction (XRD), transmission electron microscopy (TEM), XPS and Raman spectroscopy. The photocatalytic activity of the as-prepared composite materials was evaluated towards degradation of RhB under simulated sunlight and a possible mechanism of photocatalytic degradation is presented. In particular, the effect of the g-C_3N_4 content on RhB photodegradation was investigated in detail. We further explored the nonlinear optical properties of the samples at the visible spectral wavelength of 532 nm, using 4 ns laser pulses. The introduction of PPy and g-C_3N_4 yields a moderate enhancement of the nonlinearity when compared to the pristine $Bi_2O_2CO_3$. Donor–acceptor complexes can be formed when the composites are photoexcited, and nonlinearity enhancement occurs due to a combination of mechanisms. The results demonstrate that the combination of the three materials ($Bi_2O_2CO_3$, PPy and g-C_3N_4) in such a way can be a promising approach to improve the photoelectric performances, and the samples are capable of exhibiting dual functionality, both as efficient photocatalysts and optical limiters.

2. Experimental section

2.1. Materials and reagents

Pyrrole monomer (C_4H_4NH, analytical grade) was provided by Shanghai Sinopharm Chemical Reagent Co. Ltd, China, which was distilled under reduced pressure until it became colorless and stored under nitrogen in dark before use. Tetrahydrofuran (THF) were dried over metallic sodium and distilled before use. All other chemicals were of chemical and analytical grade used as received unless otherwise stated. Deionized water was used throughout the materials preparation process. g-C_3N_4 was prepared according to the literature as reported.[29]

2.2. Characterization

The as-prepared $Bi_2O_2CO_3$/PPy/g-C_3N_4 nanocomposites were characterized by using different techniques. Fourier-transform infrared (FTIR) spectra of the samples were collected on a MB154S-FTIR spectrometer (Bomem, Canada) at room temperature using spectroscopic grade KBr pellets in the range 4000–400 cm^{-1}. X-ray powder diffraction (XRD) analysis was performed at room temperature by means of a XD-3 diffractometer (Beijing Purkinje General Instrument Co. Ltd, China) using Cu Kα radiation ($\lambda = 0.15418$ nm) in the scanning range from 10° to 80° at a rate of 3° min^{-1}. Transmission electron microscopy (TEM) experiments were carried out by using a JEM-2100 (JEOL) instrument working at 200 kV. The samples were thoroughly dispersed in ethanol. Then a drop of a dilute dispersion of the as-prepared products was coated on amorphous carbon-coated copper grids and then dried in air before it was transferred into the TEM sample chamber. Raman spectra were measured on a Renishaw Invia Raman Microscope with Ar+ radiation (532 nm); the laser light was focused onto samples by using a microscope equipped with a 100× objective. Energy dispersive X-ray spectroscopy (EDS) was also done for further chemical analysis using a JSM7001F (JEOL) equipped with an Oxford Instruments INCA system. X-ray photoelectron spectroscopy (XPS) analyses were performed on a RBD upgraded PHI-5000C ESCA (Perkin-Elmer) electron spectrometer with a Mg Kα line at 280 eV. Surface areas of the as-prepared samples were measured using Brunauer–Emmett–Teller (BET) method performed on a NOVA 2000e instrument. Pore size distributions were determined by the Barrett–Joyner–Halenda (BJH) method using adsorption data. Prior to the measurements, the samples were degassed at 150 °C for 3 h under vacuum. UV-Vis diffuse spectra were recorded using a Varian Cary 500 spectrophotometer at room temperature in the range 200–800 nm by using $BaSO_4$ pellet as a reflectance standard. The fluorescence spectra were recorded on a Fluoro-Max-P spectrofluorimeter.

2.3. Measurement of photocatalytic activity

The photocatalytic activities of the samples were evaluated by the photocatalytic degradation of rhodamine (RhB) in aqueous solution under simulated light irradiation at room temperature. A 350 W Xe-lamp (Nanshen Company, Shanghai) was used as simulated sunlight source, which is located *ca.* 20 cm above the sample dish. In a typical procedure, some catalyst (*ca.* 50 mg)

was suspended in 50 mL RhB aqueous solution (0.5 mM, pH value: 7) in a Pyrex reactor surrounded by circulating water to cool the lamp. Prior to irradiation, the suspension was stirred in the dark for about 15 min to reach the adsorption balance between the organic molecules and the catalyst surface. At given irradiation time intervals, about 3.0 mL of the reaction suspension was collected, and immediately separated by centrifugation; the RhB concentration after illumination was determined at *ca.* 554 nm by using a UV-vis spectrophotometer.

2.4. Electrochemical measurements

The photoelectrochemical measurements of the as-prepared samples were carried out in an aqueous solution containing 0.2 M Na_2SO_4 with an electrochemical workstation (CHI 614D, CH Instrument). Working electrodes were prepared as follows: the as-prepared samples (20 mg) and Nafion solution (5 wt%, 40 μL) were dispersed in 0.5 mL of water/ethanol (4/1, v/v) by ultrasonication (ultrasonic probe, 2 mm diameter, 130 W, 2 h) to form homogeneous ink. Then 40 μL of the catalyst ink was dropped onto the indium tin oxide (ITO) substrate. Next, these electrodes were dried in an oven at 60 °C for 30 min. A three-electrode configuration was employed in the measurements, with the as-prepared samples covered ITO as the working electrode, a Pt wire (1×1 cm^2) as the counter electrode, and a silver/silver chloride (Ag/AgCl) electrode as the reference electrode. The ITO substrate covered with samples was assembled into a homemade Teflon electrochemical cell, with a defined area (0.7854 cm^2) of the front surface of sample exposing to electrolyte during measurements. For photoelectrochemical measurements, a xenon lamp (350 W) was utilized as the light source, and the incident density of illumination was adjusted to 100 mW cm^{-2} before each experiment. The transient photocurrent measurement was performed at a constant potential of 0.95 V *vs.* Ag/AgCl. Electrochemical impedance spectroscopy was measured at an open-circuit voltage. A sinusoidal ac perturbation of 10 mV was used to the electrode over the frequency of 1 to 10^6 Hz.

2.5. Nonlinear optical measurements

The nonlinear optical property of the samples was measured by the Z-scan technique, which is widely used in optical nonlinearity, mainly due to the simplicity of the experimental setup and the easy interpretation of the results. The major advantage of this technique is that the magnitude and the sign of the nonlinearity can be provided simultaneously. The samples were dispersed in dimethylsulfoxide (DMSO) in a quartz cell of 2 mm thickness for the nonlinear optical measurements, which were performed with linearly polarized 4 ns pulsed laser radiation at 532 nm, generated from a mode-locked Nd:YAG laser with a repetition rate of 2 Hz. The optical pulses were of top-hat spatial profiles. DMSO solutions of the tested samples were positioned at the focal point ($z = 0$) of a lens with a focal length of 40 cm and the cells were then moved along the axis of the incident beam (z-direction) with respect to the focal point. Since the sample experiences different incident laser energy at each position as it moving along the z direction, any nonlinearity in transmission can be revealed by this measurement. The energy of the input (laser energy reaching the sample) and output (laser energy exiting the sample) laser pulses was monitored simultaneously by two energy detectors (Rjp-765 energy probe), which were linked to a computer by a GPIB interface. To measure the nonlinear absorption of the samples, the Z-dependent transmittance was measured by using the open-aperture Z-scan method. In this technique, the aperture is absent, and so the total transmitted energy is detected, from which the nature of the absorptive optical nonlinearity can be determined alone. Division of the Z-scan curve obtained with an aperture by that without an aperture gives a curve with nonlinear absorption effectively eliminated, and affords the nonlinear refraction response.

2.6. Preparation of nanocomposites

2.6.1. Preparation of $Bi_2O_2CO_3$/PPy nanocomposites. PPy was prepared according to the reported method.[8] $Bi_2O_2CO_3$ nanosheets were obtained by using a hydrothermal method modified from a previous work.[30] Briefly, bismuth nitrate pentahydrate (0.96 g), trisodium citrate dihydrate (1.76 g) and urea (0.48 g) was mixed with 30 mL deionized H_2O and sonicated for 30 min at room temperature to obtain a homogeneous suspension. The resulting mixture was transferred into a 50 mL Teflon-lined stainless autoclave and heated at 200 °C for 24 h. Upon cooling to room temperature, the as-obtained precipitates were filtered, washed thoroughly with deionized H_2O several times, rinsed with EtOH, and then dried under vacuum at room temperature for 12 h to produce a white powder of $Bi_2O_2CO_3$. The $Bi_2O_2CO_3$/PPy (BP) nanocomposites were prepared as follows: the obtained $Bi_2O_2CO_3$ (200 mg) and PPy (2 mg) were added into THF (20 mL), subjected to ultrasound for 2 h, and then stirred for 24 h under reflux. Finally, the suspension was centrifuged and washed by deionized H_2O and EtOH, and then dried under vacuum at room temperature for 12 h. For the purpose of comparison, the $Bi_2O_2CO_3$/g-C_3N_4 (B/C0.5) composites with 0.5 wt% g-C_3N_4 were also prepared by the same method.

2.6.2. Preparation of $Bi_2O_2CO_3$/PPy/C_3N_4 nanocomposites. In a typical procedure, the as-prepared BP composites (80 mg) were first sonicated in THF (20 mL) for 1 h, and then a certain amount of g-C_3N_4 was added to the above solution and stirred for another 1 h to obtain a homogenous suspension. Subsequently, the mixture solution was treated by refluxing for 12 h. After be cooled down to room temperature naturally, the resultant materials were collected, washed with EtOH and deionized water for several times. At last, the obtained samples were dried under vacuum at room temperature for 12 h. To investigate the effect of g-C_3N_4 on the photocatalytic degradation of the RhB solution, the weight percentage of g-C_3N_4 to the BP composites was varied from 0.1 to 2.0 (*e.g.* 0.1, 0.25, 0.5, 1.0, 1.5, 2.0 wt%), and the corresponding samples were labeled as BP/C0.1, BP/C0.25, BP/C0.5, BP/C1.0, BP/C1.5, and BP/C2.0, respectively.

3. Results and discussion

3.1. Structure, composition and morphology

FTIR spectroscopy was carried out to confirm the composition of samples. Fig. 1 displays the FTIR spectra of all the prepared

samples. In the case of the pristine $Bi_2O_2CO_3$, two intensive peaks at 1389 and 1469 cm^{-1} are ascribed to the antisymmetric vibrational mode ν_3 of the CO_3^{2-} group, while the peaks at 845 cm^{-1} is assigned to the out-of-plane bending mode ν_2 of the CO_3^{2-} group.[31] Moreover, the absorption band at 549 cm^{-1} is attributed to the stretching mode of the Bi–O–Bi group.[32] For the $Bi_2O_2CO_3$/PPy/C_3N_4 composites, the characteristic bands corresponding to $Bi_2O_2CO_3$ still remain, but the typical absorption peaks of PPy and g-C_3N_4 decrease dramatically in intensity or even disappear when compared to those of the pure PPy (for comparative purpose, the FTIR spectrum of PPy is also provided (Fig. S1 in ESI†)) and g-C_3N_4, which may be due to their low content in the composites. It is obvious that no impurities were detected, indicating the high purity of the $Bi_2O_2CO_3$/PPy/C_3N_4 composites. Similar results are also observed for BP and B/C0.5. Raman spectroscopy is an efficient way to detect the purity and the structure of the composite with high sensitivity. Fig. 2 shows the Raman spectra of the $Bi_2O_2CO_3$, BP, B/C0.5 and BP/C0.5 samples. For pure $Bi_2O_2CO_3$, the strong bands below 600 cm^{-1} are mainly due to lattice vibration.[30] The intense Raman band at 165 cm^{-1} is attributed to the external vibration mode of the carbonate ion, and the band at 355 cm^{-1} probably results from the motion of oxygen atoms in the polymeric $(BiO)_n^{n+}$ cation.[33] The small band at 665 cm^{-1} in the Raman spectrum is indexed to the internal vibration ν_4 of the CO_3^{2-} group. The band at 1072 cm^{-1} is assigned to the internal vibration ν_1 of the CO_3^{2-} group. Two bands at 1374 and 1469 cm^{-1} are indexed to the internal vibration ν_3 of the CO_3^{2-} group.[34] When compared to $Bi_2O_2CO_3$, a down-shift (5 cm^{-1}) corresponding to the external vibration mode of the carbonate ion was observed for BP. While the bands in the region 1200–1800 cm^{-1} show notable broadening relative to $Bi_2O_2CO_3$, as a consequence of the introduction of PPy (for comparative purpose, the Raman spectrum of PPy is also provided (Fig. S2 in ESI†)). In the case of the BP/C0.5 composite, a similar down-shift can also be observed in comparison to BP. Furthermore, a new peak was observed for BP/C0.5 in the region 1200–1800 cm^{-1} when compared to BP and $Bi_2O_2CO_3$, resulting from the doping of C_3N_4 (for comparative purpose, the Raman spectrum of g-C_3N_4 is also provided (Fig. S3 in ESI†)). Indeed, a broad band is also found for B/C0.5 due to the introduction of g-C_3N_4. All above results demonstrated the successful combination of the $Bi_2O_2CO_3$ and PPy together with g-C_3N_4 in a single system.

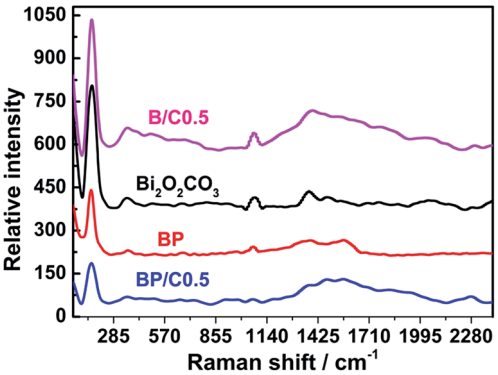

Fig. 2 Raman spectra of $Bi_2O_2CO_3$, BP, B/C0.5 and BP/C0.5.

The crystal quality of the as-prepared samples was analyzed by XRD, the results being shown in Fig. 3. All the diffraction peaks can be readily indexed to the standard diffraction data of tetragonal $Bi_2O_2CO_3$ (JCPDS no. 41-1488). For $Bi_2O_2CO_3$, the main diffraction peak positions appear at 13.05°, 23.98°, 30.42°, 32.79°, 42.46°, 47.10°, 52.3° and 56.99°, which correspond to the (002), (011), (013), (110), (114), (020), (017) and (123) lattice planes of $Bi_2O_2CO_3$.[14] No characteristic peaks from other crystalline impurities can be observed, implying that the sample is highly pure. The XRD patterns of the BP, B/C0.5 and BP/C0.5 samples exhibit almost the same peak positions and shapes although with different intensities, suggesting that the modification of $Bi_2O_2CO_3$ with PPy and g-C_3N_4 did not influence the lattice structure of $Bi_2O_2CO_3$. In particular, no diffraction peaks attributed to PPy and g-C_3N_4 (for comparative purpose, the XRD patterns of PPy and g-C_3N_4 are also provided (Fig. S4 in ESI†)) can be observed, which also indicates that the amount of PPy and g-C_3N_4 is small, and is consistent with results of FTIR spectra. The intense and relatively sharp diffraction peaks imply the well crystallization of the samples. In addition, it should be noted that the intensity ratio of the (110) peak to the (013) peak of $Bi_2O_2CO_3$ is higher than the standard value (0.386), indicating the anisotropic growth of $Bi_2O_2CO_3$ along the (110) plane.[35]

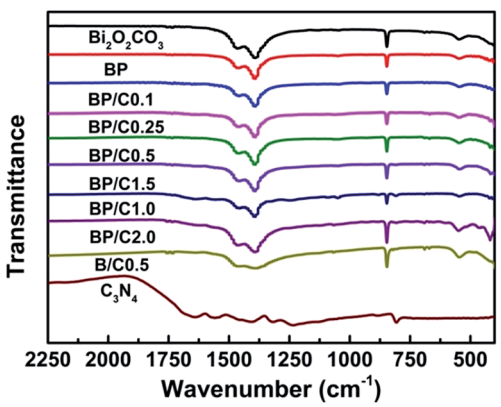

Fig. 1 FTIR spectra of the as-prepared samples.

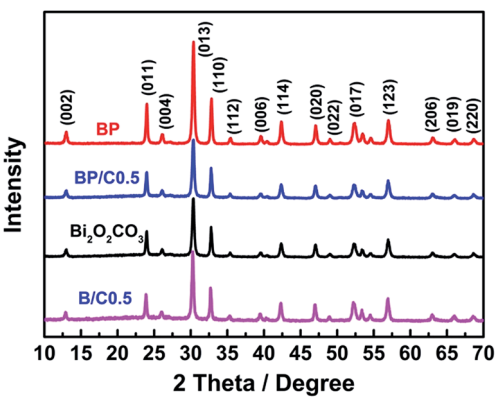

Fig. 3 XRD patterns of $Bi_2O_2CO_3$, BP, B/C0.5 and BP/C0.5.

The structure and morphologies of the as-prepared samples were further inspected with TEM. The obtained results are shown in Fig. 4 (for comparative purpose, the TEM spectra of PPy, g-C_3N_4 and B/C0.5 are also provided (Fig. S5 in ESI†)). Fig. 4a shows the typical TEM image of pure $Bi_2O_2CO_3$. It can be seen that the $Bi_2O_2CO_3$ products are composed of large scale, irregular platelet-like nanoplates with width of nanometer. For the sample BP (Fig. 4b), the rodlike PPy polymers (darker part) are visible on the $Bi_2O_2CO_3$ surface (brighter part). For the BP/C0.5 composites (Fig. 4c), the platelet-like $Bi_2O_2CO_3$, rodlike PPy and sheet-like g-C_3N_4 can be observed. Fig. 4d displays the EDS analysis of the BP/C0.5 composites. The samples contain bismuth, oxygen, carbon and nitrogen, confirming the formation of final BP/C0.5 composites. The elemental composition is corresponding to $Bi_2O_2CO_3$, g-C_3N_4 and PPy. XPS analysis was carried out on the BP/C0.5 composites to further determine the surface chemical composition. The survey XPS spectrum (Fig. 5a) displays that the main elements on the surface of the sample are bismuth, oxygen, carbon and nitrogen. The asymmetrical and broad features of the observed C 1s XPS peaks (Fig. 5b) indicate the co-existence of distinguishable models.[30,36,37] The curve fitting suggests chemically different C species in BP/C0.5 composites, with four C 1s binding energy peaks located at *ca.* 284.48, 285.08, 288.58, and 289.18 eV, respectively. The peak at 284.48 and 285.08 eV could be ascribed to the C–C and C=C functional groups and the peak with binding energy of 288.58 indicated the presence of sp^2 C atoms bonded to aliphatic amine (–NH_2 or –NH–) in the aromatic rings,[38–40] while the peak observed at 289.18 eV is close to the literature value of the carbon of carbonate in $Bi_2O_2CO_3$.[41] The results of XPS analysis was in accordance with the EDS measurement, which further confirmed the coexistence of $Bi_2O_2CO_3$, PPy and g-C_3N_4 in the BP/C0.5 materials. The $Bi_2O_2CO_3$ and PPy attach on the g-C_3N_4 surface to assemble the BP/C0.5 composites. Actually, the layered nature favors the self-assembly of the units to form the characteristic platelet-like nanostructure of the materials. However, the $Bi_2O_2CO_3$ and PPy assembled onto the g-C_3N_4 are not uniform (Fig. 4), and there is a stacking of irregular nanoplates on the surface of the sheet-like g-C_3N_4. The deposition of two-dimensional (2D) $Bi_2O_2CO_3$ and PPy on the surface of 2D g-C_3N_4 nanoplates may induce tight contact. The BP composite can interact with the g-C_3N_4 sheets through physisorption, electrostatic binding and

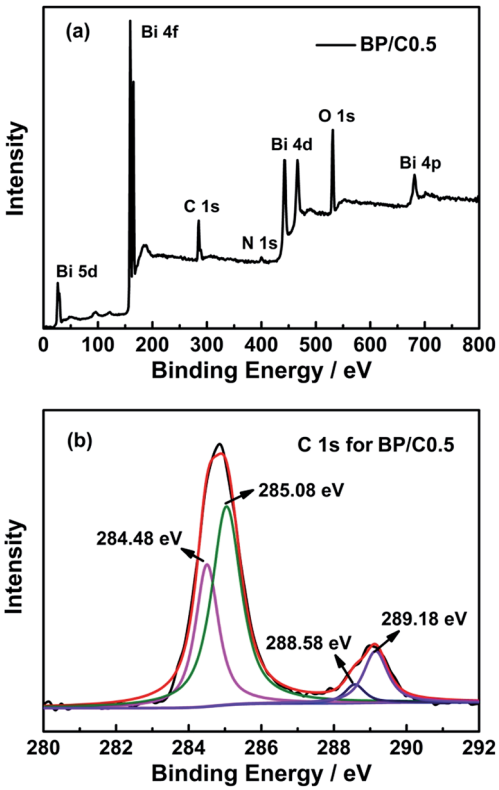

Fig. 5 Survey XPS spectra (a) and high-resolution XPS spectra (b) of the as-prepared BP/C0.5.

charge transfer interactions.[42] As a result, the close interaction may enable fast transfer of electrons during photo-excitation processes. In addition, lager contact area can be obtained through the formation of three-component nanojunction system, which is expected to offer more adsorption sites. All of these would be beneficial to the transferring of charges, and may induce higher separation efficiency of photo-generated electron–hole pairs, thus enhance the photocatalytic activity.

3.2. Photocatalytic performance

g-C_3N_4 hybridized BP nanocomposites with different mass ratios from 0.1% to 2.0% were prepared to investigate the effect of g-C_3N_4 loading amount on the photocatalytic performances, which are denoted as BP/C0.1, BP/C0.25, BP/C0.5, BP/C1.0, BP/

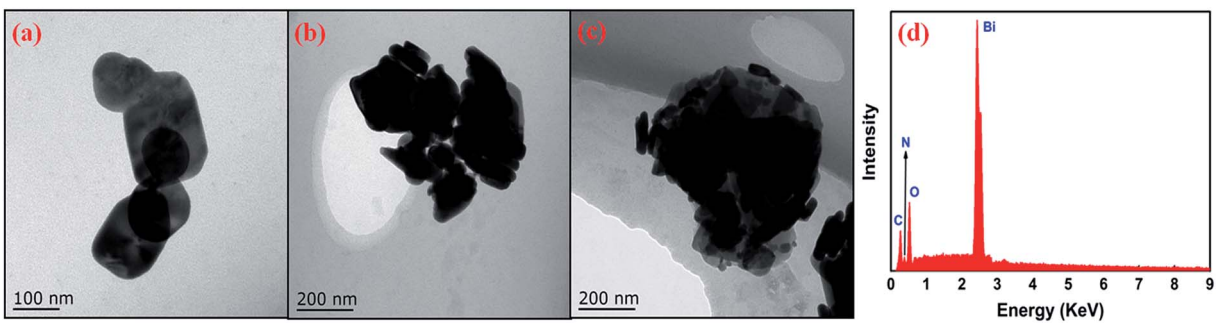

Fig. 4 TEM images of (a) $Bi_2O_2CO_3$, (b) BP, and (c) BP/C0.5, and (d) EDS spectrum of BP/C0.5.

C1.5, and BP/C2.0, respectively. The photocatalytic performance of the as-prepared samples is investigated for the photodegradation of RhB under simulated sunlight irradiation after the adsorption–desorption equilibrium between the sample and RhB was achieved. Fig. 6 shows the temporal evolution of RhB concentration by the spots of C/C_0 *versus* irradiation time in the presence of the as-prepared samples, where C is the concentration of the rest RhB, and C_0 is the concentration of RhB solution after adsorption equilibrium. Before studying and comparing the activities of the as-prepared samples, the bleaching of RhB in the absence of any catalysts was first examined. Control experiment results suggest that the RhB degradation performance could be ignored in the absence of photocatalyst, suggesting that RhB is degraded *via* photocatalytic process.[43] In addition, it seems very important to consider whether photocatalysis could still happen effectively after the adsorption of RhB to the as-prepared samples reached equilibrium. For $Bi_2O_2CO_3$, only 46.6% of RhB can be photodegraded after 90 min irradiation, but about 62.8% of RhB was photodegraded for BP under the same conditions. This may be due to the rapid electron hole separation and slow recombination efficiency resulting from the synergic effect of PPy and $Bi_2O_2CO_3$.[14] The adding of g-C_3N_4 can dramatically influence the photoreactivity of BP. It can be found that the efficiency on the degradation of RhB by the prepared samples under simulated sunlight was quite different. The photocatalytic activities of the BP/C samples are a function of the mass ratios between g-C_3N_4 and BP. The photocatalytic activity increases with the increasing of g-C_3N_4 loading content from 0.1% to 0.5%. Further increase in g-C_3N_4 loading content leads to a decrease in the photocatalytic activity and negative trend was observed. For example, when the loading content of g-C_3N_4 is 1.5%, a dramatic decrease was observed in the photocatalytic activity. As expected, all of the BP/C composites exhibited higher activity than the pristine $Bi_2O_2CO_3$. As the mass ratio of g-C_3N_4/BP increases to 0.5%, the highest photocatalytic efficacy is achieved and RhB was almost completely degraded after 90 min of simulated sunlight irradiation. In particular, the photocatalytic efficacy of BP/C0.5 is larger than those of BP and B/C0.5. All these results clearly confirm that the photocatalytic activity of $Bi_2O_2CO_3$ can be significantly enhanced through coupling with a suitable amount of PPy and g-C_3N_4. Our results are in agreement with previous studies,[44,45] in which suitable g-C_3N_4 content is crucial for optimizing the photocatalytic performance of the BP/C nanocomposites.

For a better understanding of the photocatalytic efficiency at various illumination times, the photodegradation process of RhB was investigated by the UV-vis absorption spectra. Fig. 7 displays the time dependent spectroscopic changes occurred in the dyes catalyzed by using BP/C0.5 under light irradiation. It is clearly seen that the absorption band of RhB decreased gradually with a blue shift during photocatalytic degradation, which indicates cleavage of the whole conjugated structure in the degradation process, corresponding to the stepwise formation of a series of N-deethylated intermediates.[46] Correspondingly, the pink color of the starting RhB solutions gradually faded during the process of photodegradation (not shown). The absorption maximum of these intermediates located at 554–505 nm in the visible spectral region. The photodegradation efficiencies of BP/C0.5 were found to increase gradually with increasing irradiation time, reaching the maximum degradation efficiency of 98.94% after 90 min. Most importantly, for the photodegradation of RhB by BP/C0.5, the peak intensity in the UV region (250 nm < λ < 370 nm) also decreased upon increasing irradiation time. This further suggests that the chromophoric structure of the dye was decomposed.

Based on the key principles of green chemistry, the effective catalysis and catalytic recovery were crucial to feasibility of the wastewater treatment process. Thus, estimating the recyclable performance of photocatalyst is indispensable for its possible continuous use in the practical applications of the BP/C0.5 composites. The separated photocatalysts were washed with deionized water and dried after every 90 min of photodegradation. Fig. 8 shows the photocatalytic stabilities of BP/C0.5 evaluated in a recycle test of five runs under identical conditions. As shown in Fig. 8, during the first 2 cycles, the photocatalytic degradation efficiency was 98.94% and 97.85%, respectively. The catalytic activity slightly dropped in runs 3 and 4, giving 95.62% and 94.60% degradation efficiency, respectively. In the 5th run, the catalyst exhibited 92.61% degradation efficiency. The lowering of photocatalytic efficiency may be due

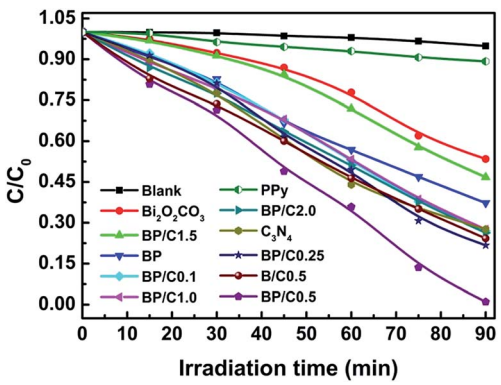

Fig. 6 Photocatalytic performances of the as-prepared samples for the photodegradation of RhB aqueous solutions under ambient conditions. The relative standard deviation is less 0.65%.

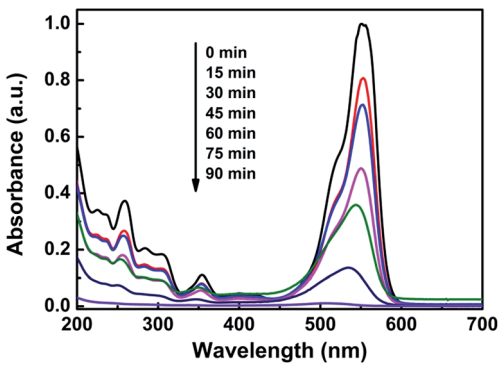

Fig. 7 UV-vis spectral changes of RhB aqueous solutions in the presence of the BP/C0.5 sample as a function of the irradiation time.

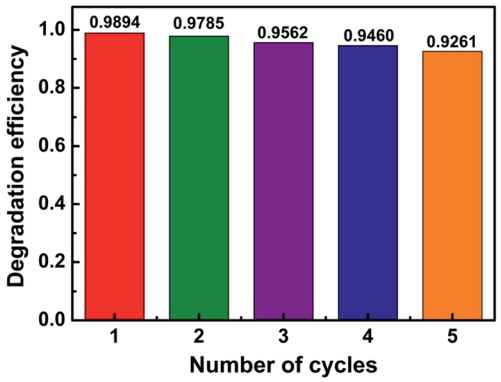

Fig. 8 The photocatalytic stabilities of RhB degradation over BP/C0.5.

not only to some leaching of active component and/or weight loss during the repeated filtration process to separate the catalyst from RhB solution, but also to the accumulation of residual RhB in the inner pores.[13,42,47] The results indicate that the as-prepared BP/C0.5 sample remains effective after five cycles within a relative standard deviation of 0.76%, and therefore it is basically stable for the photosensitized degradation of organic pollutants under simulated sunlight irradiation and promising for environmental remediation.

3.3. Possible mechanism of photocatalytic activity enhancement

To probe the mechanism on the enhancement of photocatalytic activity for the BP/C0.5 composites, several experiments are carried out. The good photocatalytic efficiency may be ascribed to three factors. First of all, surface area of a nanomaterial is closely related to the number of adsorption sites as well catalytic activities, which is an indispensable factor in photocatalysis.[48] The specific surface area and porosity of the as-prepared samples were investigated by nitrogen adsorption–desorption measurement. As shown in Fig. 9, a typical IV isotherm with H3-type hysteresis is observed for all samples, indicating that the existence of mesoporous structure.[49] The specific surface area of BP, B/C0.5 and BP/C0.5 were calculated to be 11.469, 15.065, and 17.142 $m^2 g^{-1}$, respectively, which are larger than pure $Bi_2O_2CO_3$ (7.753 $m^2 g^{-1}$). The large surface area of BP/C0.5 benefiting from the special hierarchical structure is expected to accelerate the photocatalytic activity by providing more active sites and promoting the separation efficiency of photocarriers. In addition, the Barrett–Joyner–Halenda (BJH) method was employed to determine the pore size distributions of $Bi_2O_2CO_3$, BP, B/C0.5, and BP/C0.5. The pore size distribution is monomodal for all samples. The mesoporous in the samples most likely originated from their inter-nanosheet spacing, which is in accordance with the TEM analysis.

Second, the improved light-harvesting ability can be considered to be one major reason for the superior photocatalytic performance of the BP/C0.5 sample.[50] The light absorption property of g-C_3N_4, $Bi_2O_2CO_3$, BP, B/C0.5 and BP/C0.5 is investigated by UV-vis diffuse reflectance spectra (for comparative purpose, the UV-vis diffuse reflectance spectrum of PPy is also provided (Fig. S6 in ESI†)). As shown in Fig. 10, The pure $Bi_2O_2CO_3$ displays significant light absorption in the UV region, and has almost no absorption at $\lambda > 350$ nm. However, a slight red shift in the UV region and an obvious absorption in the visible light region were observed for BP compared to $Bi_2O_2CO_3$, which may lead to a possible charge-transfer transition at the interface between PPy and $Bi_2O_2CO_3$.[14] As a consequence, the BP composites can be easier to produce electron–hole pairs under the same light irradiation and exhibit improved photocatalytic performance. However, only a slight change was observed for B/C0.5 when compared to $Bi_2O_2CO_3$. The pristine g-C_3N_4 exhibits a fundamental absorption edge at 450 nm, originating from the charge transfer response of g-C_3N_4 from the valence band populated by N 2p orbital to the conduction band formed by C 2p orbital.[51] After the introduction of g-C_3N_4 in the BP composites, the visible absorption intensities of the BP/C0.5 composites are obviously enhanced and the absorption edge also displays a slight red shift, which may allow for more utilization of the solar spectrum to produce photogenerated electrons and holes.

Third, the charge separation and migration also play a very important role on the photocatalytic reaction process.[52] Thus, the photocurrent response and electrochemical impedance experiments were performed to investigate the photogenerated

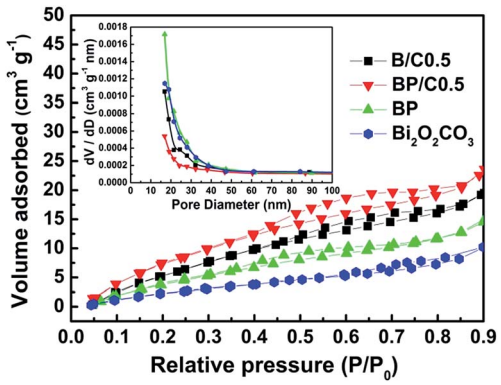

Fig. 9 Nitrogen adsorption–desorption isotherms and the corresponding pore-size distribution curves (inset) of $Bi_2O_2CO_3$, BP, B/C0.5 and BP/C0.5.

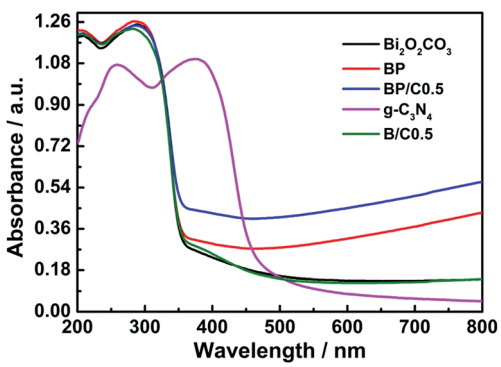

Fig. 10 UV-vis diffuse reflection spectra of g-C_3N_4, $Bi_2O_2CO_3$, BP, B/C0.5 and BP/C0.5.

charge carrier behaviors. Fig. 11 shows the photocurrent responses of $Bi_2O_2CO_3$, BP, g-C_3N_4, PPy, B/C0.5 and BP/C0.5 after deposition on ITO under the simulated sunlight irradiation. The rise and fall of the photocurrent response are apparent for each switch-on/off cycle in all the electrodes ($Bi_2O_2CO_3$, BP, g-C_3N_4, PPy, B/C0.5 and BP/C0.5). The photocurrent transients have different shape for each electrode. As forecasted, the weak photocurrent density of pure $Bi_2O_2CO_3$ can be detected due to the large energy gap.[53] In contrast to $Bi_2O_2CO_3$, PPy and g-C_3N_4, the BP, B/C0.5 and BP/C0.5 composites exhibit a remarkably enhanced photocurrent response. By comparison, the highest photocurrent intensity was observed for BP/C0.5, which is about 3.75 times as high as that of $Bi_2O_2CO_3$ and 1.75 times of BP. The trend of photocurrent intensity is clearly consistent with the photocatalytic activity. The increased photocurrent intensity implies that more electrons are transferred to photoelectrode, indicating greater separation of the photoinduced electrons and holes.[12,47,54]

Fig. 12 shows the electrochemical impedance spectra Nyquist plots of pure BiO_2CO_3, BP and BP/C0.5 composites. The arc radii of BP/C0.5 electrode are much smaller than those of $Bi_2O_2CO_3$ and BP electrodes. It should be noted that the large arc radius observed for the electrode is indicative of a high interfacial charge-transfer resistance, due to the poor electrical conductivity of materials, whereas the smaller arc radius corresponds to an electrode closer to the ideal capacitor.[30,55] Thus, the reduced arc radius for BP/C0.5 indicates diminished resistance of working electrodes, implying a decrease in the solid state interface layer resistance. Furthermore, the arc radius on the electrochemical impedance spectra Nyquist plot also reveals reaction rate occurring at the surface of the electrodes.[56] It is therefore that a more effective separation of photogenerated electron–hole pairs and a faster interfacial charge transfer occurs on BP/C0.5 surface under this condition, agreeing well with the photocurrent measurements. The efficiency of charge trapping and recombination of photoinduced electron–hole pairs for the as-prepared samples is further investigated by the photoluminescence spectra, which is of importance to evaluate the photocatalytic response of the semiconductor materials. A low photoluminescence intensity is generally indicative of a high

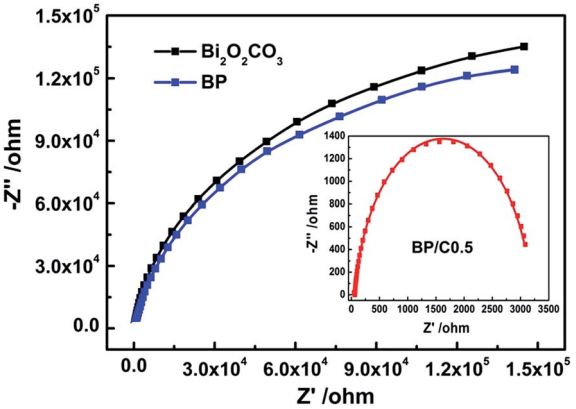

Fig. 12 Electrochemical impedance spectra of $Bi_2O_2CO_3$, BP and BP/C0.5.

separation efficiency of electron–hole pairs.[57,58] As shown in Fig. 13, the similar photoluminescence peaks were observed for the as-prepared samples (BiO_2CO_3, BP and BP/C0.5). Specifically, BP/C0.5 exhibits an obviously decreased emission signal when compared to BiO_2CO_3 and BP. These results demonstrate that the introduction of g-C_3N_4 and PPy in BiO_2CO_3 really decreases the carrier recombination rate and improves the separation efficiency of photogenerated electrons and holes. So the high photocatalytic performance of BP/C0.5 can be ascribed to the efficient separation of electron–hole pairs.

According to the above experimental results, the enhanced photocatalytic performance of the BP/C0.5 composites can be ascribed to the combined effect of several factors. In the case of PPy, two ways can be presented to explain the enhanced photon efficiency.[14] On the one hand, PPy as a hole acceptor may produce a series of actives species on its surface under simulated sunlight irradiation.[13] On the other hand, the high mobility of charge carriers can be expected in the circulatory system of BP/C0.5. As a semiconducting material, PPy could absorb the UV light, producing photogenerated carriers and consequently induced electron transition from the highest occupied molecular orbital to the lowest unoccupied molecular orbital, while the holes will

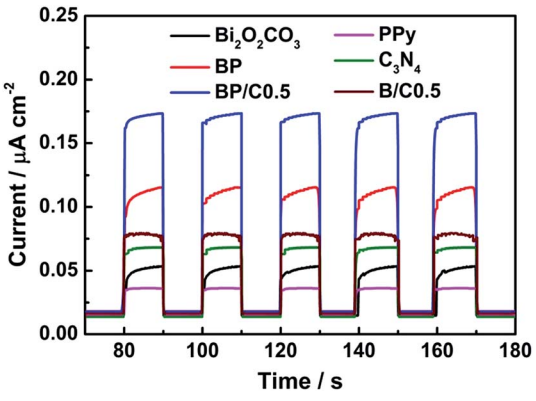

Fig. 11 The photocurrent responses of $Bi_2O_2CO_3$, BP, g-C_3N_4, PPy, B/C0.5 and BP/C0.5.

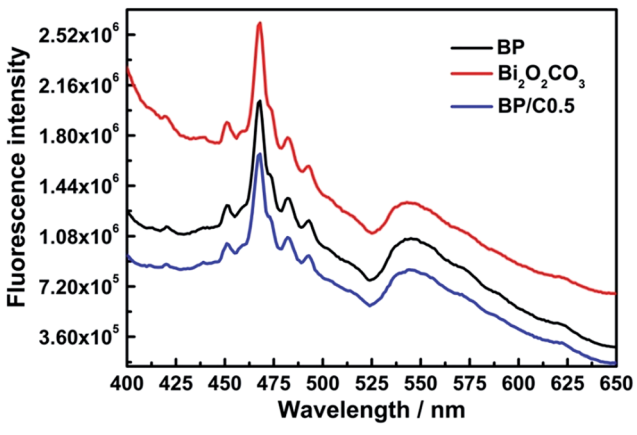

Fig. 13 Photoluminescence spectra of the pure $Bi_2O_2CO_3$, BP and BP/C0.5 samples upon excitation at 360 nm.

be left in the highest occupied molecular orbital of PPy.[59] The electrons in the valence band of BiO_2CO_3 can migrate to the highest occupied molecular orbital of PPy to recombine with holes, and the holes are generated in the valence band of BiO_2CO_3. For g-C_3N_4, it can be excited by the simulated sunlight and produce photogenerated electrons and holes.[60] Similar to PPy, the weak holes excited from g-C_3N_4 could also be quickly transferred to $Bi_2O_2CO_3$, which is faster than the electron–hole recombination between the valence band and conduction band of g-C_3N_4.[43] Then the photogenerated electrons and holes could annihilate at $Bi_2O_2CO_3$. That is to say the $Bi_2O_2CO_3$ paired between the g-C_3N_4 and PPy can participate in the transition process of the photogenerated charge carrier. Meanwhile, the strong reductive photoelectrons would be left on the conduction band of PPy, and the strong oxidizing holes would be left on the valence band of g-C_3N_4. It is therefore that the photogenerated electron–holes pairs will be separated effectively in the circulatory system of BP/C0.5, and the recombination of electron–hole pairs can be reduced, which favor the interfacial charge transfer. The separated electrons and holes are then free to initiate reactions with the reactants adsorbed on the photocatalyst surfaces, resulting in enhanced photocatalytic performance of the BP/C0.5 composites.

3.4. Nonlinear optical properties

The efficient separation of electron–hole pairs and charge transfer implies that these nanostructures are candidates for optical limiting applications.[18,25] Nonlinear optical responses can arise from charge-transfer complexes due to the possibility of excited absorption, free carrier absorption, exciton absorption, multiphoton absorption and nonlinear scattering, which can give rise to reverse saturable absorption effects in optical limiting.[27,61] To assess this possibility, Z-scan experiments employing 4 ns laser pulses at 532 nm have been performed on the $Bi_2O_2CO_3$, BP and BP/C0.5 samples dispersed in DMSO. To facilitate comparison, all sample concentrations were adjusted to 0.2 mg mL^{-1}.

Fig. 14 contains the open-aperture Z-scan traces of $Bi_2O_2CO_3$, BP and BP/C0.5 using 4 ns laser pulses. As shown in Fig. 14, all samples display decreased transmittances as they are brought closer to the focal point ($z = 0$), the extent of the reduction varying with the on-focus intensity, which is consistent with a strong nonlinear optical absorptive effect with 4 ns laser pulse excitation. The valleys of the transmittance scans indicate that laser pulses experience a strong reverse absorption behavior in all of the tested samples, typical of an induced positive nonlinear absorption of incident light.[62,63] Materials exhibiting such performance are suitable candidates as optical limiters for protection of eyes and optical sensors from intense laser pulses. For an optical limiter, the depth of the valley in the open-aperture Z-scan data is in line with the optical limiting merit.[64] Although efficient nonlinear optical properties were observed for the three samples, the greater decreased valley observed for BP/C0.5 among the transmittance curves indicate that it should have the best optical limiting performance. In addition, when the PPy is lightly introduced to $Bi_2O_2CO_3$, the

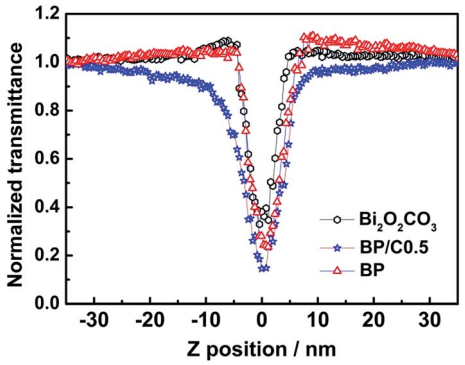

Fig. 14 Open-aperture Z-scan traces of $Bi_2O_2CO_3$, BP and BP/C0.5 in DMSO, obtained under 4 ns, 532 nm laser excitation.

nonlinear optical absorption efficiency of the resultant composite (BP) is somewhat improved, but not so remarkably.

The nonlinear refractive components were investigated by dividing the normalized Z-scan data obtained from the closed-aperture configuration, the results being shown in Fig. 15. The prefocal valley followed by postfocal peak indicates that the sign of refractive index is positive, corresponding to a self-focusing effect and thus positive nonlinearity.[65] Observation of negative nonlinearity upon excitation with ns pulses is common and is ascribed to the thermal effects generated by high fluence of ns laser pulses, so the origin of the self-focusing effect for the three samples is other than the thermal effect.[66] The positive nonlinear refraction may be assigned to the population transitions among the singlet states, the refraction volume of the singlet excited state is larger than that of the ground state.[65] It is clear that the differences between the normalized transmittance values and valley positions for BP/C0.5 and BP are larger than that of $Bi_2O_2CO_3$, indicating that the BP/C0.5 and BP composites possess larger nonlinear refraction response than the pristine $Bi_2O_2CO_3$ (Fig. 15), presumably a result of the introduction of PPy and g-C_3N_4. Particularly, the BP/C0.5 composites possess larger nonlinear refractive index than BP, which is consistent with the results of nonlinear optical absorption response (Fig. 14).

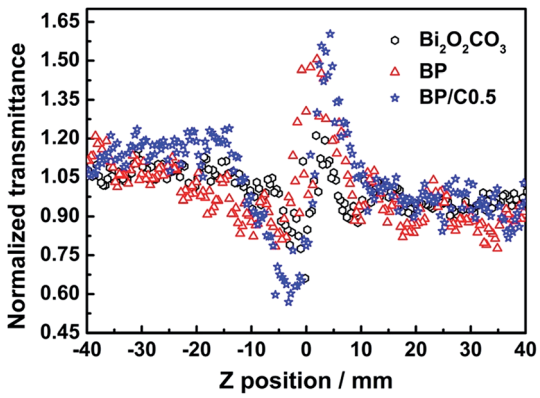

Fig. 15 Closed-aperture Z-scan traces of $Bi_2O_2CO_3$, BP and BP/C0.5 in DMSO, with 4 ns pulse durations.

Because $Bi_2O_2CO_3$, BP and BP/C0.5 exhibit significant linear absorption at the excitation wavelength (532 nm) used in the Z-scan experiment, which can be evident from the UV-visible absorption spectra (Fig. 10), the efficient nonlinear optical performance may be more reasonable to be ascribed to the photo-induced free carrier (hole–electron pairs) absorption generated by interband transitions.[61,67] When the samples are excited with the nanosecond laser beams at 532 nm, interband transitions will generate free carriers in the lowest unoccupied molecular orbital level. The generated free carriers have a tendency to absorb additional photons through a photon-assisted process, and thus a strong nonlinear optical response is facilitated through this free carrier absorption phenomenon.[25,68] In addition, besides the free carrier absorption, we have observed nonlinear scattering performance in the nanosecond regime exhibited by the BP/C0.5 composites, and we think the contribution is minimal since it is not as dominant as seen in other nanostructures like graphene suspensions.[69] Similar to nonlinear scattering, the reverse absorption performance originating from PPy and g-C_3N_4 may also play a role to somewhat for the improved optical nonlinearity,[24,25] though their content is very low in the as-prepared composites. Another possible reason for the enhanced nonlinear optical performance for BP/C0.5 in comparison to those of $Bi_2O_2CO_3$ and BP may be assigned to an intersystem excitation transfer mechanism, typical *via* the effective charge transfer process, contributes to increasing the free carrier population,[70] and this results in the fluorescence quenching and energy releasing, and therefore the limiting action. The effective charge transfer process can be supported by the results of fluorescence, photocurrent response and electrochemical impedance experiments (Fig. 11–13). Therefore, the improved nonlinear optical performances for the BP/C0.5 composites should arise from a combination of mechanisms.

4. Conclusions

In this work, a series of novel $Bi_2O_2CO_3$/PPy/g-C_3N_4 composites loaded with different g-C_3N_4 contents was prepared by a facile refluxing process, and characterized by FTIR, XRD, Raman, XPS and TEM. Sensitization of $Bi_2O_2CO_3$ with PPy and g-C_3N_4 broadened the light absorption range of $Bi_2O_2CO_3$, which has been utilized for photocatalytic and optical limiting studies. Among the as-prepared samples, the BP/C0.5 composites exhibit the highest photocatalytic performance, and a total photodegradation efficiency of 98.94% towards RhB was achieved within 90 min. In addition, g-C_3N_4 loadings larger than 0.5% result in a decrease in photocatalytic activity. The improved photocatalytic activity of BP/C0.5 can be ascribed mainly to its better light absorption property, large surface area and efficient separation efficiency of photogenerated electron–hole pairs, which are demonstrated by the results of nitrogen adsorption–desorption isotherms, UV-vis diffuse reflectance spectra, fluorescence, photocurrent response and electrochemical impedance experiments. The composite photocatalysts could be effectively recycled and re-used for five times without significant change in photocatalytic performance, which evidenced the catalyst stability as well as the repeatability of the present approach. The viability of the $Bi_2O_2CO_3$/PPy/g-C_3N_4 composites as nonlinear optical materials has been examined using the Z-scan technique at 532 nm with 4 laser ns pulses. The BP/C0.5 composites are found to exhibit enhanced nonlinear optical properties compared to $Bi_2O_2CO_3$ and BP due to a combination of mechanisms. This composite is a promising candidate for optical limiting, solar-energy conversion and storage applications. This work opens new possibilities to provide some insights into the design of novel nanoscale stable materials with photocatalytic and optical limiting properties.

Acknowledgements

This research was supported financially by the National Key Technology Support Program (2015BAD21B06), the National Natural Science Foundation of China (51506077, 21171076, 51602130), the Natural Science Foundation of Jiangsu Province (BK20150488), the Natural Science Foundation of Jiangsu High School (15KJB430007, 15KJB610003, 15KJD150002, 16KJD430002), the China Postdoctoral Foundation (2016M601733) and Research Foundation of Jiangsu University (13JDG066, 15JDG156, 1283300004).

References

1 Y. S. Xu and W. D. Zhang, Anion exchange strategy for construction of sesame-biscuit-like $Bi_2O_3CO_3/Bi_2MoO_6$ nanocomposites with enhanced photocatalytic activity, *Appl. Catal., B*, 2013, **140–141**, 306–316.

2 Y. Bai, L. Q. Ye, L. Wang, X. Shi, P. Q. Wang, W. Bai and P. K. Wong, g-$C_3N_4/Bi_4O_5I_2$ heterojunction with I^{3-}/I^- redox mediator for enhanced photocatalytic CO_2 conversion, *Appl. Catal., B*, 2016, **194**, 98–104.

3 Y. L. Zhang, D. Y. Li, Y. G. Zhang, X. F. Zhou, S. J. Guo and L. B. Yang, Graphene-wrapped $Bi_2O_2CO_3$ core-shell structures with enhanced quantum efficiency profit from an ultrafast electron transfer process, *J. Mater. Chem. A*, 2014, **2**, 8273–8280.

4 J. L. Lv, K. Dai, J. F. Zhang, L. Geng, C. H. Liang, Q. C. Liu, G. P. Zhu and C. Chen, Facile synthesis of Z-scheme graphitic-C_3N_4/Bi_2MoO_6 nanocomposite for enhanced visible photocatalytic properties, *Appl. Surf. Sci.*, 2015, **358**, 377–384.

5 D. Yuan, L. Y. Huang, Y. P. Li, Y. G. Xu, H. Xu, S. Q. Huang, J. Yan, M. Q. He and H. M. Li, Synthesis and photocatalytic activity of g-C_3N_4/BiOI/BiOBr ternary composites, *RSC Adv.*, 2016, **6**, 41204–41213.

6 Z. L. Ni, Y. J. Sun, Y. X. Zhang and F. Dong, Fabrication, modification and application of $(BiO)_2CO_3$-based photocatalysts: A review, *Appl. Surf. Sci.*, 2016, **365**, 314–335.

7 T. Xiong, H. W. Huang, Y. J. Sun and F. Dong, In situ synthesis of a C-doped $(BiO)_2CO_3$ hierarchical self-assembly effectively promoting visible light photocatalysis, *J. Mater. Chem. A*, 2015, **3**, 6118–6127.

8 P. Madhusudan, J. R. Ran, J. Zhang, J. G. Yu and G. Liu, Novel urea assisted hydrothermal synthesis of hierarchical $BiVO_4$/

$Bi_2O_2CO_3$ nanocomposites with enhanced visible-light photocatalytic activity, *Appl. Catal., B*, 2011, **110**, 286–295.

9 C. M. Li, G. Chen, J. X. Sun, Y. J. Feng and H. J. Dong, Ultrathin nanoflakes constructed erythrocyte-like Bi_2WO_6 hierarchitecture via anionic self-regulation strategy for improving photocatalytic activity and gas-sensing property, *Appl. Catal., B*, 2015, **163**, 415–423.

10 Y. H. Ao, L. Y. Xu, P. F. Wang, C. Wang, J. Hou, J. Qian and Y. Li, Graphene and TiO_2-modified flower-like $Bi_2O_2CO_3$: A novel multi-heterojunction photocatalyst with enhanced photocatalytic activity, *Appl. Surf. Sci.*, 2015, **355**, 411–418.

11 J. Q. Li, H. Yuan and Z. F. Zhu, Photoelectrochemical performances of g-C_3N_4/Au/$BiPO_4$ Z-scheme composites to improve the mineralization property under solar light, *RSC Adv.*, 2016, **6**, 70563–70572.

12 M. Yan, F. F. Zhu, W. Gu, L. Sun, W. D. Shi and Y. Q. Hua, Construction of nitrogen-doped graphene quantum dots-$BiVO_4$/g-C_3N_4 Z-scheme photocatalyst and enhanced photocatalytic degradation of antibiotics under antibiotics under visible light, *RSC Adv.*, 2016, **6**, 61162–61174.

13 F. A. Harraz, A. A. Ismail, S. A. Al-Sayari and A. Al-Hajry, Novel α-Fe_2O_3/polypyrrole nanocomposite with enhanced photocatalytic performance, *J. Photochem. Photobiol., A*, 2015, **299**, 18–24.

14 Q. Z. Wang, L. H. Zheng, Y. T. Chen, J. F. Fan, H. H. Huang and B. T. Su, Synthesis and characterization of novel PPy/$Bi_2O_2CO_3$ composite with improved photocatalytic activity for degradation of Rhodamine-B, *J. Alloys Compd.*, 2015, **637**, 127–132.

15 B. C. Zhu, P. F. Xia, W. K. Ho and J. G. Yu, Isoelectric point and adsorption activity of porous g-C_3N_4, *Appl. Surf. Sci.*, 2015, **344**, 188–195.

16 J. Q. Wen, J. Xie, X. B. Chen and X. Lin, A review on g-C_3N_4-based photocatalysts, *Appl. Surf. Sci.*, 2017, **391**, 72–123.

17 L. Shi, J. L. Gou, L. Liang, F. X. Wang and J. M. Sun, The crystal phase transformation of Ag_2WO_4 through loading onto g-C_3N_4 sheets with enhanced visible-light photocatalytic activity, *RSC Adv.*, 2016, **6**, 96861–96869.

18 J. Balapanuru, J. X. Yang, S. Xiao, Q. L. Bao, M. Jahan, L. Polavarapu, J. Wei, Q. H. Xu and K. P. Loh, A graphene oxide-organic dye ionic complex with DNA-sensing and optical limiting properties, *Angew. Chem., Int. Ed.*, 2010, **49**, 6549–6553.

19 Y. F. Xu, Z. B. Liu, X. L. Zhang, Y. Wang, J. G. Tian, Y. Huang, Y. F. Ma, X. Y. Zhang and Y. S. Chen, A graphene hybrid material covalently functionalized with porphyrin: Synthesis and optical limiting property, *Adv. Mater.*, 2009, **21**, 1275–1279.

20 J. H. Zhu, Y. X. Li, Y. Chen, J. Wang, B. Zhang, J. J. Zhang and W. J. Blau, Graphene oxide covalently functionalized with zinc phthalocyanine for broadband optical limiting, *Carbon*, 2011, **49**, 1900–1905.

21 A. P. R. Mary, C. S. S. Sandeep, T. N. Narayanan, R. Philip, M. Padraig, P. M. Ajayan and M. R. Anantharaman, Nonlinear and magneto-optical transmission studies on magnetic nanofluids of non-interacting metallic nickel nanoparticles, *Nanotechnology*, 2011, **22**, 375702.

22 G. L. Chai, C. S. Lin, J. Wei, M. Y. Zhang and W. D. Cheng, Nonlinear optical properties of carbon nitride nanotubes, *Phys. Chem. Chem. Phys.*, 2012, **14**, 835–839.

23 H. W. Huang, N. Tian, S. F. Jin, Y. H. Zhang and S. B. Wang, Syntheses, characterization and nonlinear optical properties of a bismuth subcarbonate $Bi_2O_2CO_3$, *Solid State Sci.*, 2014, **30**, 1–5.

24 A. J. Wang, W. Zhao and W. Yu, Effect of acid/base on the third-order optical nonlinearity of polypyrrole, *J. Mol. Struct.*, 2015, **1099**, 291–296.

25 K. Sridharan, P. Sreekanth, T. J. Park and R. Philip, Nonlinear optical investigations in nine-atom silver quantum clusters and graphitic carbon nitride nanosheets, *J. Phys. Chem. C*, 2015, **119**, 16314–16320.

26 S. Abed, K. Bouchouit, M. S. Aida, S. Taboukhat, Z. Sofiani, B. Kulyk and V. Figa, Nonlinear optical properties of zinc oxide doped bismuth thin films using Z-scan technique, *Opt. Mater.*, 2016, **56**, 40–44.

27 K. Sridharan, T. Kuriakose, R. Philip and T. J. Park, Transition metal (Fe, Co and Ni) oxide nanoparticles grafted graphitic carbon nitrides as efficient optical limiters and recyclable photocatalysts, *Appl. Surf. Sci.*, 2014, **308**, 139–147.

28 M. R. Gholipour, G. T. Dinh, F. Béland and T. O. Do, Nanocomposite heterojunctions as sunlight-driven photocatalysts for hydrogen production from water splitting, *Nanoscale*, 2015, **7**, 8187–8208.

29 X. Wang, K. Maeda, A. Thomas, K. Takanabe, G. Xin, J. M. Carlsson, K. Domen and M. Antonietti, A metal-free polymeric photocatalyst for hydrogen production from water under visible light, *Nat. Mater.*, 2009, **8**, 76–80.

30 P. Madhusudan, J. G. Yu, W. G. Wang, B. Cheng and G. Liu, Facile synthesis of novel hierarchical graphene-$Bi_2O_2CO_3$ composites with enhanced photocatalytic performance under visible light, *Dalton Trans.*, 2012, **41**, 14345–14353.

31 W. L. Cen, T. Xiong, C. Y. Tang, S. D. Yuan and F. Dong, Effects of morphology and crystallinity on the photocatalytic activity of $(BiO)_2CO_3$ nano/microstructures, *Ind. Eng. Chem. Res.*, 2014, **53**, 15002–15011.

32 N. Tian, H. W. Huang, Y. X. Guo, Y. He and Y. H. Zhang, A g-C_3N_4/$Bi_2O_2CO_3$ composite with high visible-light-driven photocatalytic activity for rhodamine B degradation, *Appl. Surf. Sci.*, 2014, **322**, 249–254.

33 R. Keuleers, H. O. Desseyn, B. Rousseau and C. Van Alsenoy, Vibrational analysis of urea, *J. Phys. Chem. A*, 1999, **103**, 4621–4630.

34 G. E. Tobon-Zapata, S. B. Etcheverry and E. J. Baran, Vibrational spectrum of bismuth subcarbonate, *J. Mater. Sci. Lett.*, 1997, **16**, 656–657.

35 H. Cheng, B. Huang, K. Yang, Z. Wang, X. Qin, X. Zhang and Y. Dai, Facile template-free synthesis of $Bi_2O_2CO_3$ hierarchical microflowers and their associated photocatalytic activity, *ChemPhysChem*, 2010, **11**, 2167–2173.

36 J. Di, J. X. Xia, Y. Huang, M. X. Ji, W. M. Fan, Z. G. Chen and H. M. Li, Constructing carbon quantum dots/Bi_2SiO_5 ultrathin nanosheets with enhanced photocatalytic activity

and mechanism investigation, *Chem. Eng. J.*, 2016, **302**, 334–343.

37 J. Di, J. X. Xia, M. X. Ji, L. Xu, S. Yin, Q. Zhang, Z. G. Chen and H. M. Li, Carbon quantum dots in situ coupling to bismuth oxyiodide via reactable ionic liquid with enhanced photocatalytic molecular oxygen activation performance, *Carbon*, 2016, **98**, 613–623.

38 Y. Z. Hong, C. S. Li, G. Y. Zhang, Y. D. Meng, B. X. Yin, Y. Zhao and W. D. Shi, Efficient and stable Nb_2O_5 modified g-C_3N_4 photocatalyst for removal of antibiotic pollutant, *Chem. Eng. J.*, 2016, **299**, 74–84.

39 J. X. Xia, M. X. Ji, J. Di, B. Wang, S. Yin, Q. Zhang, M. Q. He and H. M. Li, Construction of ultrathin C_3N_4/$Bi_4O_5I_2$ layered nanojunctions via ionic liquid with enhanced photocatalytic performance and mechanism insight, *Appl. Catal., B*, 2016, **191**, 235–245.

40 S. Q. Huang, Y. G. Xu, M. Xie, H. Xu, M. Q. He, J. X. Xia, L. Y. Huang and H. M. Li, Synthesis of magnetic CoFe2O4/g-C3N4 composite and its enhancement of photocatalytic ability under visible-light, *Colloids Surf., A*, 2015, **478**, 71–80.

41 Z. Y. Zhao, Y. Zhou, F. Wang, K. H. Zhang, S. Yu and K. Cao, Polyaniline-decorated {001} facets of $Bi_2O_2CO_3$ nanosheets: In situ oxygen vacancy formation and enhanced visible light photocatalytic activity, *ACS Appl. Mater. Interfaces*, 2015, **7**, 730–737.

42 M. Xiong, L. Chen, Q. Yuan, J. He, S. L. Luo, C. T. Au and S. F. Yin, Facile fabrication and enhanced photosensitized degradation performance of the g-C_3N_4-$Bi_2O_2CO_3$ composite, *Dalton Trans.*, 2014, **43**, 8331–8337.

43 Q. Zhang, H. Y. Wang, S. Z. Hu, G. Lu, J. Bai, X. X. Kang, D. Liu and J. Z. Gui, Synthesis and properties of visible light responsive g-C_3N_4/$Bi_2O_2CO_3$ layered herterojunction nanocomposites, *RSC Adv.*, 2015, **5**, 42736–42743.

44 X. J. Wang, Q. Wang, F. T. Li, W. Y. Yang, Y. Zhao, Y. J. Hao and S. J. Liu, Novel BiOCl-C_3N_4 heterojunction photocatalysts: In situ preparation via an ionic-liquid-assisted solvent-thermal route and their visible-light photocatalytic activities, *Chem. Eng. J.*, 2013, **234**, 361–371.

45 C. S. Pan, J. Xu, Y. J. Wang, D. Li and Y. F. Zhu, Dramatic activity of C_3N_4/$BiPO_4$ photocatalyst with core/shell structure formed by self-assembly, *Adv. Funct. Mater.*, 2012, **22**, 1518–1524.

46 Y. S. Xu, Z. J. Zhang and W. D. Zhang, Facile preparation of heterostructured Bi_2O_3/Bi_2MoO_6 hollow microspheres with enhanced visible-light-driven photocatalytic and antimicrobial activity, *Mater. Res. Bull.*, 2013, **48**, 1420–1427.

47 D. Wang, Y. Xu, F. Sun, Q. H. Zhang, P. Wang and X. Y. Wang, Enhanced photocatalytic activity of TiO_2 under sunlight by MoS_2 nanodots modification, *Appl. Surf. Sci.*, 2016, **377**, 221–227.

48 J. Di, J. X. Xia, M. X. Ji, B. Wang, S. Yin, H. Xu, Z. G. Chen and H. M. Li, Carbon quantum dots induced ultrasmall BiOI nanosheets with assembled hollow structures for broad spectrum photocatalytic activity and mechanism insight, *Langmuir*, 2016, **32**, 2075–2084.

49 J. Di, J. X. Xia, X. W. Li, M. X. Ji, H. Xu, Z. G. Chen and H. M. Li, Constructing confined surface carbon defects in ultrathin graphitic carbon nitride for photocatalytic free radical manipulation, *Carbon*, 2016, **107**, 1–10.

50 W. B. Li, C. Feng, S. Y. Dai, J. G. Yue, F. X. Hua and H. Hou, Fabrication of sulfur-doped g-C_3N_4/Au/CdS Z-scheme photocatalyst to improve the photocatalytic performance under visible light, *Appl. Catal., B*, 2015, **168–169**, 465–471.

51 S. W. Cao, J. X. Low, J. G. Yu and M. Jaroniec, Polymeric photocatalysts based on graphitic carbon nitride, *Adv. Mater.*, 2015, **27**, 2150–2176.

52 K. H. Ye, Z. S. Cha, J. W. Gu, X. Yu, C. X. Zhao, Y. M. Zhang and W. J. Mai, BiOI-$BiVO_4$ photoanodes with significantly improved solar water splitting capability: p–n junction to expand solar adsorption range and facilitate charge carrier dynamics, *Nano Energy*, 2015, **18**, 222–231.

53 Z. Y. Wang, Y. Huang, W. K. Ho, J. J. Cao, Z. X. Shen and S. C. Lee, Fabrication of $Bi_2O_2CO_3$/g-C_3N_4 heterojunctions for efficiently photocatalytic NO in air removal: In-situ self-sacrificial synthesis, characterizations and mechanistic study, *Appl. Catal., B*, 2016, **199**, 123–133.

54 G. P. Dai, J. G. Yu and G. Liu, Synthesis and enhanced visible-light photoelectrocatalytic activity of p–n junction BiOI/TiO_2 nanotube arrays, *J. Phys. Chem. C*, 2011, **115**, 7339–7346.

55 J. Xu, Y. J. Wang and Y. F. Zhu, Nanoporous graphitic carbon nitride with enhanced photocatalytic performance, *Langmuir*, 2013, **29**, 10566–10572.

56 F. C. Lei, Y. F. Sun, K. T. Liu, S. Gao, L. Liang, B. C. Pan and Y. Xie, Oxygen vacancies confined in ultrathin indium oxide porous sheets for promoted visible-light water splitting, *J. Am. Chem. Soc.*, 2014, **136**, 6826–6829.

57 Y. H. Ao, J. Q. Bao, P. F. Wang, C. Wang and J. Hou, Bismuth oxychloride modified titanium phosphate nanoplates: A new p–n type heterostructured photocatalyst with high activity for the degradation of different kinds of organic pollutants, *J. Colloid Interface Sci.*, 2016, **476**, 71–78.

58 X. Zhang, P. Zhang, L. J. Wang, H. Q. Gao, J. T. Zhao, C. H. Liang, J. H. Hu and G. S. Shao, Template-oriented synthesis of monodispersed SnS_2@SnO_2 hetero-nanoflowers for Cr(VI) photoreduction, *Appl. Catal., B*, 2016, **192**, 17–25.

59 H. Zhang, R. L. Zong, J. C. Zhao and Y. F. Zhu, Dramatic visible photocatalytic degradation performances due to synergetic effect of TiO_2 with PANI, *Environ. Sci. Technol.*, 2008, **42**, 3803–3807.

60 Y. B. Li, H. M. Zhang, P. R. Liu, D. Wang, Y. Li and H. J. Zhao, Cross-linked g-C_3N_4/rGO nanocomposites with tunable band structure and enhanced visible light photocatalytic activity, *Small*, 2013, **9**, 3336–3344.

61 L. W. Tutt and T. F. Boggess, A review of optical limiting mechanisms and devices using organics, fullerenes, semiconductors and other materials, *Prog. Quantum Electron.*, 1993, **17**, 299–338.

62 J. Y. Yang, Y. L. Song, W. J. Zhu, X. Y. Su and H. Y. Xu, Investigation of optical nonlinearities and transient dynamics in a stilbenzene derivative, *J. Phys. Chem. B*, 2012, **116**, 1221–1225.

63 G. H. Li, A. J. Wang, J. B. Song and Q. Zhou, A novel zinc tetraphenylporphyrinate substituted in the axial position with one E-stilbazole: Synthesis, structure, and nonlinear optics, *Inorg. Chem. Commun.*, 2015, **57**, 47–50.

64 Z. Guo, F. Du, D. M. Ren, Y. S. Chen, J. Y. Zheng, Z. B. Liu and J. G. Tian, Covalently porphyrin-functionalized single-walled carbon nanotubes: a novel photoactive and optical limiting donor-acceptor nanohybrid, *J. Mater. Chem.*, 2016, **16**, 3021–3030.

65 L. Jiang, T. G. Jiu, Y. L. Li, Y. B. Li, J. Y. Yang, J. B. Li, C. H. Li, H. B. Liu and Y. L. Song, Excited-state absorption and sign tuning of nonlinear refraction in porphyrin derivatives, *J. Phys. Chem. B*, 2008, **112**, 756–759.

66 B. Shanmugavelu, V. V. R. K. Kumar, R. Kuladeep and D. N. Rao, Third order nonlinear optical properties of bismuth zinc borate glasses, *J. Appl. Phys.*, 2013, **114**, 243103.

67 M. Molli, S. Parola, L. A. A. Chunduri, S. Aditha, V. S. Muthukumar, T. M. Rattan and V. Kamisetti, Solvothermal synthesis and study of nonlinear optical properties of nanocrystalline thallium doped bismuth telluride, *J. Solid State Chem.*, 2012, **189**, 85–89.

68 R. Philip, P. Chantharasupawong, H. Qian, R. Jin and J. Thomas, Evolution of nonlinear optical properties: From gold atomic clusters to plasmonic nanocrystals, *Nano Lett.*, 2012, **12**, 4661–4667.

69 J. Wang, Y. Hernandez, M. Lotya, J. N. Coleman and W. J. Blau, Broadband nonlinear optical response of graphene dispersions, *Adv. Mater.*, 2009, **21**, 2430–2435.

70 S. Kumar, E. S. Shibu, T. Pradeep and A. K. Sood, Ultrafast photoinduced enhancement of nonlinear optical response in 15-atom gold clusters on indium tin oxide conducting film, *Opt. Express*, 2013, **21**, 8483–8492.

